

# Detection of single photons by toad and mouse rods

Jürgen Reingruber<sup>a</sup>, Johan Pahlberg<sup>b</sup>, Michael L. Woodruff<sup>c</sup>, Alapakkam P. Sampath<sup>b</sup>, Gordon L. Fain<sup>c</sup>, and David Holcman<sup>a,1</sup>

<sup>a</sup>Institut de Biologie de l'École Normale Supérieure, Group of Computational Biology and Applied Mathematics, École Normale Supérieure, 75005 Paris, France; <sup>b</sup>Department of Physiology and Biophysics, Zilkha Neurogenetic Institute, University of Southern California, Los Angeles, CA 90089; and <sup>c</sup>Department of Integrative Biology and Physiology, University of California, Los Angeles, CA 90095-7239

Edited\* by John E. Dowling, Harvard University, Cambridge, MA, and approved October 15, 2013 (received for review July 26, 2013)

**Amphibian and mammalian rods can both detect single photons of light even though they differ greatly in physical dimensions, mammalian rods being much smaller in diameter than amphibian rods. To understand the changes in physiology and biochemistry required by such large differences in outer segment geometry, we developed a computational approach, taking into account the spatial organization of the outer segment divided into compartments, together with molecular dynamics simulations of the signaling cascade. We generated simulations of the single-photon response together with intrinsic background fluctuations in toad and mouse rods. Combining this computational approach with electrophysiological data from mouse rods, we determined key biochemical parameters. On average around one phosphodiesterase (PDE) molecule is spontaneously active per mouse compartment, similar to the value for toad, which is unexpected due to the much smaller diameter in mouse. A larger number of spontaneously active PDEs decreases dark noise, thereby improving detection of single photons; it also increases cGMP turnover, which accelerates the decay of the light response. These constraints explain the higher PDE density in mammalian compared with amphibian rods that compensates for the much smaller diameter of mammalian disks. We further find that the rate of cGMP hydrolysis by light-activated PDE is diffusion limited, which is not the case for spontaneously activated PDE. As a consequence, in the small outer segment of a mouse rod only a few activated PDEs are sufficient to generate a signal that overcomes noise, which permits a shorter lifetime of activated rhodopsin and greater temporal resolution.**

phototransduction | mathematical modeling | analysis | stochastic

Signal transduction at a single molecular level requires controlled biochemical events occurring in constrained cellular microdomains. Furthermore, intrinsic fluctuations in the events of the transduction pathway generate a noisy background, which sets the limit of detection. Of all of the G-protein cascades in nature, the best understood are those initiated by the absorption of a photon in *Drosophila* microvilli (1, 2) and in the outer segment (OS) of vertebrate rod photoreceptors (1, 3, 4). Much of the research on vertebrate transduction has used either amphibians or mammals. The rods of both species have been shown to have the remarkable ability to detect single photons of light above background noise (5, 6); and for both a photon closes about 5% of the channels open in darkness. However, amphibian and mammalian rods differ in concentrations and biochemical properties of proteins involved in the light response and by as much as an order of magnitude in the diameter of their disk membranes, where the reactions of the cascade take place. It remains largely unknown how the biochemistry and the rod geometry adapt to guarantee a reliable macroscopic response initiated by a single molecular event.

To explore this fundamental question, we developed a model that combines spatially resolved reaction–diffusion equations that account for the subcellular organization of a rod OS, with molecular dynamics simulations that reproduce the variability in the biochemistry. The major source of noise during a single-photon response is produced by fluctuations in the activity of the critical enzyme phosphodiesterase (PDE). PDE fulfills two essential functions. First, the PDE that becomes activated through the

transduction cascade after a photon absorption (light-activated PDE) increases the hydrolysis of cGMP, a diffusible second messenger controlling the opening of ionic membrane channels, leading to channel closure and cell hyperpolarization; second, spontaneously activated PDE is necessary to maintain in darkness a steady-state cGMP concentration and to set the cGMP turnover rate (7, 8). Fluctuations in the number of spontaneously activated PDEs generate the dark noise (7, 9, 10). The main source of variability in the amplitude of the single-photon response is due to variability in the number of light-activated PDEs (6, 11–13). By simulating PDE activations and cGMP hydrolysis at the level of single molecules, we generated realistic simulations of the dark noise and the single-photon response that can be directly compared with experimental recordings.

We used toad and mouse rods as model systems to study the effect of differences in the biochemistry and the outer segment geometry on the single-photon response. From electrophysiological recordings of GCAPs<sup>-/-</sup> knockout mice we extracted the rates for spontaneous activation and deactivation of PDE in a mouse rod. We found that cGMP hydrolysis by spontaneously and light-activated PDE proceeds in mouse with very different rate constants. We show that the differences in outer segment geometry between mouse and toad can explain why mammalian rods have a higher concentration of PDE and are able to respond with greater temporal resolution, while preserving sensitivity to single photons above background noise.

## Methods and Theory

To study the photon response and the intrinsic noise, we developed a mathematical model by combining spatially resolved reaction–diffusion equations with stochastic simulations of PDE activations at the level of single molecules. Previous models used Markov chains to account for the stochastic nature of the biochemistry (14, 15) or partial differential equations to capture the complex OS geometry (16–19), but here we unify these approaches into a single model. We further derive expressions for the dark noise power spectrum, which we use to estimate the values of key parameters from the analysis of dark current recordings in WT and GCAPs<sup>-/-</sup> knockout mice. We now summarize our model, and a detailed description is given in *SI Appendix*.

## Significance

**Amphibian and mammalian rods both detect single photons of light even though mammalian rods are much smaller in diameter. To understand how this is possible, we combined electrical recordings with computations. We show that changes in the rod diameter go hand in hand with changes in the biochemistry to allow for single-photon detection.**

Author contributions: J.R., A.P.S., G.L.F., and D.H. designed research; J.R., J.P., M.L.W., and D.H. performed research; J.R. and D.H. analyzed data; and J.R., G.L.F., and D.H. wrote the paper.

The authors declare no conflict of interest.

\*This Direct Submission article had a prearranged editor.

<sup>1</sup>To whom correspondence should be addressed. E-mail: holcman@biologie.ens.fr.

This article contains supporting information online at [www.pnas.org/lookup/suppl/doi:10.1073/pnas.1314030110/-DCSupplemental](http://www.pnas.org/lookup/suppl/doi:10.1073/pnas.1314030110/-DCSupplemental).

**Coarse Graining of the Outer Segment Geometry.** The OS geometry consists of nearly separate compartments formed by the spaces between the disks, labeled by  $n = 1, \dots, N_{comp}$  (where  $N_{comp}$  is the total number of compartments). Compartments are connected to each other only through narrow gaps between the disk rim and the plasma membrane and through incisures (*SI Appendix, Fig. S1*). The compartmentalization reduces the longitudinal diffusion of cGMP and calcium between compartments, whereas transversal diffusion within a compartment is not hindered and produces rapid equilibration. We therefore adopt the approximation of a transversally well-stirred outer segment where the 3D geometry is incorporated in the effective parameters of a one-dimensional reaction–diffusion model (19). The main effect of disk incisures is to facilitate longitudinal diffusion (17, 18), which is accounted for by the effective longitudinal diffusion constant.

**Stochastic Model for Spontaneous PDE Activation.** To model dark noise, we performed molecular dynamics simulations of the number of spontaneously activated PDEs  $P_{sp}^*(n, t)$  in each compartment  $n$  with Poisson activation and deactivation rates  $\nu_{sp}$  and  $\mu_{sp}$  (*SI Appendix, Fig. S2*). The activation and deactivation rates produce variations that are responsible for the continuous component of rod dark noise (7, 9). The mean number of spontaneously active PDEs per compartment is

$$\bar{P}_{sp,comp}^* = 2\rho_{pde}\pi R^2\nu_{sp}/\mu_{sp}, \quad [1]$$

where  $R$  is the disk radius and  $\rho_{pde}$  is the PDE surface density. For a toad rod, with  $R = 3 \mu\text{m}$  and  $\rho_{pde} = 100 \mu\text{m}^{-2}$  from ref. 20, and  $\nu_{sp} = 4 \times 10^{-4} \text{ s}^{-1}$  and  $\mu_{sp} = 1.8 \text{ s}^{-1}$  from ref. 7, we compute  $\bar{P}_{sp,comp}^* = 1.2$ . In *SI Appendix, Fig. S1A* we show a simulation of  $P_{sp}^*(n, t)$  in a toad compartment.

**Stochastic Model for PDE Activation After Photon Absorption.** We compute the time course of the stochastic number of light-activated PDEs  $P_{li}^*(t)$  after a single-photon absorption with the G-protein–coupled PDE activation cascade analyzed in ref. 21 (6, 15). The biochemical reactions are given in *SI Appendix, Eq. 3*. Activated rhodopsin  $R^*$  becomes gradually quenched via  $N_p = 6$  phosphorylation steps and is deactivated by arrestin binding;  $R^*$  activates the G-protein transducin with phosphorylation state-dependent rates, and excited transducin binds to and activates PDE. For mouse rods, the activated rhodopsin lifetime is of the order of 40 ms (22, 23) and the PDE deactivation rate is of the order of  $5 \text{ s}^{-1}$  (23, 24). For toad rods these values are not as well determined but are likely to be of the order of 2.5 s for the rhodopsin lifetime (10, 11) and  $0.625 \text{ s}^{-1}$  for the PDE deactivation rate (11, 25) (*SI Appendix*). Simulations of  $P_{li}^*(t)$  for a toad and a mouse rod are shown in Fig. 1A (and see Fig. 4C).

**cGMP Hydrolysis by Spontaneously and Light-Activated PDE.** A key feature is the modeling of cGMP hydrolysis by individual spontaneous and light-activated PDE with different rate constants  $k_{sp}$  and  $k_{li}$ . Light-activated PDE is an extremely efficient enzyme (26), and we therefore equate  $k_{li}$  with the diffusional encounter rate  $k_{enc}$  between cGMP and an activated PDE (*SI Appendix*). The value of  $k_{enc}$  depends on the OS geometry and is computed in *SI Appendix, Eq. 6*. For a toad rod we estimate  $k_{enc} \approx 2.9 \text{ s}^{-1}$ , and for a much smaller mouse rod we find  $k_{enc} \approx 61 \text{ s}^{-1}$ , which is similar to  $43 \text{ s}^{-1}$  reported in ref. 27.

To estimate the cGMP hydrolysis rate  $k_{sp}$  of a spontaneously activated PDE we use the expression (19, 28)

$$\beta_d = k_{sp}\bar{P}_{sp,comp}^* \quad [2]$$

For toad rods the value of  $\beta_d$  has been variously estimated from  $\beta_d \sim 0.1 \text{ s}^{-1}$  up to  $\beta_d \sim 1.5 \text{ s}^{-1}$  (7, 11, 15). With  $\beta_d = 1 \text{ s}^{-1}$  and  $\bar{P}_{sp,comp}^* \approx 1.25$ , we find  $k_{sp} = 0.8 \text{ s}^{-1}$ . For a mouse rod with  $\beta_d = 4.1 \text{ s}^{-1}$  (27) and  $\bar{P}_{sp,comp}^* = 0.9$  (estimated in this work) we get  $k_{sp} = 4.5 \text{ s}^{-1}$ . In summary,  $k_{li}$  is given by the encounter rate, whereas  $k_{sp}$  is derived from Eq. 2 with estimates for  $\beta_d$  and  $\bar{P}_{sp,comp}^*$ .

**Reaction–Diffusion Equations for cGMP and Calcium.** To model the dynamics of the cGMP concentration  $g_n(t)$  in compartment  $n$ , we account for effective longitudinal diffusion, for hydrolysis and  $\text{Ca}^{2+}$ -dependent synthesis. For the dynamics of the free  $\text{Ca}^{2+}$  concentration  $ca_n(t)$  we consider effective longitudinal diffusion, exchange between the OS and the extracellular medium through channels and exchangers, and buffering. With  $g_d$  and  $ca_d$  as the mean steady-state concentrations in darkness, the scaled concentrations  $\hat{g}_n(t) = g_n(t)/g_d$  and  $\hat{ca}_n(t) = ca_n(t)/ca_d$  satisfy the equations

$$\frac{d\hat{g}_n}{dt} = d_g \Delta \hat{g}_n + \beta_d \frac{r_\alpha + (1-r_\alpha) \frac{k_\alpha^{n_\alpha}}{k_\alpha^{n_\alpha} + \hat{ca}_n^{n_\alpha}}}{r_\alpha + (1-r_\alpha) \frac{k_\alpha^{n_\alpha}}{k_\alpha^{n_\alpha} + 1}} - k_{sp} P_{sp}^*(n, t) \hat{g}_n - k_{li} P_{li}^*(n, t) \hat{g}_n \quad [3]$$

$$\frac{d\hat{ca}_n}{dt} = d_{ca} \Delta \hat{ca}_n + \gamma_d \left( \frac{(1+k_{ch}^{n_{ch}}) \hat{g}_n^{n_{ch}}}{\hat{g}_n^{n_{ch}} + k_{ch}^{n_{ch}}} - \frac{(1+k_{ex}) \hat{ca}_n}{\hat{ca}_n + k_{ex}} \right)$$

where  $\Delta \hat{g}_n = \hat{g}_{n+1} + \hat{g}_{n-1} - 2\hat{g}_n$ ,  $\Delta \hat{ca}_n = \hat{ca}_{n+1} + \hat{ca}_{n-1} - 2\hat{ca}_n$ , and the rate of calcium exchange  $\gamma_d = \frac{1}{B_{ca}} \frac{f_{ca}}{f_{ca} + 2} \frac{I_{os,d}}{ca_d V_{os,d}}$ . For the definition and values of all of the parameters we refer to *SI Appendix, Tables S1–S4*. We recall here that  $r_\alpha$  is the ratio between the minimal and maximal cGMP synthesis rate,  $B_{ca}$  is the calcium buffering capacity,  $f_{ca}$  is the fraction of the current carried by  $\text{Ca}^{2+}$ ,  $I_{os,d} = N_{comp} I_{comp,d}$  is the mean dark current,  $I_{comp,d}$  is the mean dark current associated with a single compartment, and  $V_{os} = N_{comp} V_{comp}$  is the cytosolic OS volume. A detailed derivation of these equations is given in *SI Appendix*.

**Local and Overall Currents.** The scaled currents  $\hat{I}_n(t) = I_n(t)/I_{comp,d}$  and  $\hat{I}_{os}(t) = I_{os}(t)/I_{os,d}$  are

$$\hat{I}_n(t) = \frac{2}{f_{ca} + 2} \frac{(1+k_{ch}^{n_{ch}}) \hat{g}_n^{n_{ch}}}{\hat{g}_n^{n_{ch}} + k_{ch}^{n_{ch}}} + \frac{f_{ca}}{f_{ca} + 2} \frac{(1+k_{ex}) \hat{ca}_n}{\hat{ca}_n + k_{ex}} \quad [4]$$

$$\hat{I}_{os}(t) = \frac{1}{N_{comp}} \sum_{n=1} \hat{I}_n(t).$$

Normalized currents are  $\hat{\mathcal{I}}_n(t) = 1 - \hat{I}_n(t)$  and  $\hat{\mathcal{I}}_{os}(t) = 1 - \hat{I}_{os}(t)$ .

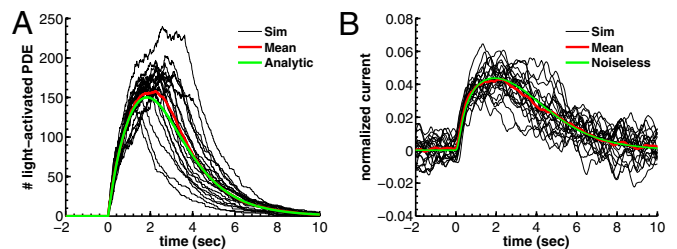


**Fig. 1.** Simulation of dark noise and single-photon response for a toad rod. (A) Twenty simulations (black) of the light-activated PDE after a photon absorption with mean (red). The analytic mean (green) is computed from ref. 21. Time, mean, SD, and coefficient of variation (CV) of the peak number are 1.85 s, 150, 25, and  $25/150 \approx 0.17$  (in agreement with predictions from figure 2e in ref. 21). (B) Superposition of 20 single-photon responses [black, normalized current  $\hat{\mathcal{I}}_{os}(t)$ ] obtained with light-activated PDE from A and with  $\beta_d = 1 \text{ s}^{-1}$ . The noiseless simulation (green) is generated with the analytic curve from A. The SD of the dark noise is around 0.8%, and the theoretical value is 0.7% (*SI Appendix, Eq. 53*). Time, mean, SD, and CV of the peak current are 1.9 s, 4.4%, 0.9%, and  $0.9/4.4 \approx 0.20$ . All parameters are given in *SI Appendix, Tables S3 and S4*.

**Power Spectrum of the Dark Noise.** We estimate kinetic parameters for a mouse photoreceptor from the power spectrum and variance analysis of continuous dark noise (7). In *SI Appendix*, we derive the expression for the power spectrum of the dark current (*SI Appendix*, Eq. 42). In a GCAPs<sup>-/-</sup> mouse rod, the power spectrum and variance simplify to ( $\xi_{ch} \approx 3$ )

$$S_{I_{os}}(\omega) = \frac{4\xi_{ch}^2}{N_{comp}\bar{P}_{sp,comp}^*} \frac{\beta_d^2 \mu_{sp}}{(\beta_d^2 + \omega^2)(\mu_{sp}^2 + \omega^2)} \quad [5]$$

$$\Sigma_{I_{os}}^2 = \frac{1}{2\pi} \int_0^\infty S_{I_{os}}(\omega) d\omega = \frac{\xi_{ch}^2}{N_{comp}\bar{P}_{sp,comp}^*} \frac{\beta_d}{\beta_d + \mu_{sp}} \quad [6]$$

## Results

**Dark Noise and Single-Photon Response in Toad Rods.** We began with toad as a test of our model, because the rates of spontaneously activated and deactivated PDEs that produce the dark noise have already been determined for this species (7). We incorporated those rates into our equations to simulate the time course of the stochastic number of spontaneously activated PDEs in each compartment (*SI Appendix*, Fig. S1A), which we subsequently used to compute the dark noise. PDE activations after a single-photon absorption reduce the photocurrent by ~5% (5, 11). Because the number of light-activated PDEs cannot be directly measured, it is unclear how many of them are generated during a photon response. Simulations from our model reveal that the answer depends strongly on the value of  $\beta_d$ . With  $\beta_d = 1 \text{ s}^{-1}$ , around 150 light-activated PDEs (Fig. 1A) are needed to produce a single photon response with an amplitude around ~5% (Fig. 1B). In contrast, with  $\beta_d = 0.5 \text{ s}^{-1}$  (*SI Appendix*, Fig. S8) only around 60 light-activated PDEs are needed to produce responses that are almost indistinguishable from the ones shown in Fig. 1B. In addition to this, the number of light-activated PDEs is also somewhat dependent on the properties of calcium feedback (*SI Appendix*, Fig. S9). Despite these uncertainties, the results in Fig. 1 show that previously determined rates of PDE activation and deactivation can be used with our model to simulate single-photon responses similar to those actually recorded (see, for example, figure 1B in ref. 11).

**Dark Noise Analysis for GCAPs<sup>-/-</sup> Mouse Rods.** We next turned to mouse. We first extracted the values of the parameters  $\mu_{sp}$  and  $\bar{P}_{sp,comp}^*$  for mouse rods. We then simulated the dark noise and compared the result with experimental data. The value of  $\nu_{sp}$  was computed from Eq. 1 with  $R = 0.7 \text{ }\mu\text{m}$  and  $\rho_{pde} = 500 \text{ }\mu\text{m}^{-2}$  (20). We used electrophysiological recordings from GCAPs<sup>-/-</sup> mice because the dark noise level is larger than in wild-type mice and less affected by instrumental noise (29–31). In addition, there is no  $\text{Ca}^{2+}$  feedback to guanylyl cyclase (32). To separate physiological from instrumental and channel noise, we performed voltage-clamp patch recordings in dark-adapted and saturating light conditions with recording durations between 5 s and 15 s (*Materials and Methods*). We used patch recording instead of suction-electrode recording because instrumentation noise was smaller and noise measurements were more consistent. In Fig. 2A, we show the concatenated currents (scaled by the measured dark current) recorded in darkness and bright light from 15 GCAPs<sup>-/-</sup> rods. The power spectrum in bright light, composed entirely of instrumental and channel noise, was subtracted from the spectrum in darkness to obtain the dark–light (or difference) power spectrum (7).

For GCAPs<sup>-/-</sup> rods, the expression for the power spectrum divided by the variance (Eqs. 5 and 6) reduces to a double Lorentzian that depends only on  $\mu_{sp}$  and  $\beta_d$ . With  $\beta = 4.1 \text{ s}^{-1}$  (27), we were left with a single unknown parameter that we estimated by fitting for each rod the dark–light spectrum scaled by the dark–light variance, and we found  $\mu_{sp} = 12 \pm 3.7 \text{ s}^{-1}$  ( $n = 15$

rods, see *SI Appendix* for more details). We further generated a long current trace by joining the individual recordings scaled by the rod-specific dark currents (Fig. 2B). From this longer current we computed a somewhat smoother spectrum and obtained a similar value of  $\mu_{sp} = 12.8 \text{ s}^{-1}$ . Subsequently, we used these values of  $\mu_{sp}$  to compute  $\bar{P}_{sp,comp}^*$  from Eq. 6 [with  $N_{comp} = 810$  (20)] and we obtained  $\bar{P}_{sp,comp}^* = 0.9 \pm 0.42$  and  $\bar{P}_{sp,comp}^* = 0.94$ , respectively. To simulate the dark noise in a GCAP<sup>-/-</sup> rod (Fig. 2B), we used the averaged value  $\mu_{sp} = 12.4 \text{ s}^{-1}$  and  $\bar{P}_{sp,comp}^* = 0.9$ . We quantified the agreement between experiment and simulation by comparing the probability distributions of the recorded and simulated current amplitudes (Fig. 2C) and by comparing the experimental dark–light spectrum with the simulated and analytical power spectra (Fig. 2D).

**Dark Noise Analysis for Wild-Type Mouse Rods.** To simulate noise in a WT rod, we used  $\mu_{sp}$  and  $\bar{P}_{sp,comp}^*$  obtained from GCAPs<sup>-/-</sup> rods. These values alone are not sufficient to simulate the dark noise in a WT rod due to the significant impact of calcium feedback, which depends on buffering and calcium regulation of cGMP synthesis (29, 31). We accounted for calcium dynamics by adjusting the buffering capacity  $B_{ca}$  and the parameter  $r_{ca}$ , which control the calcium feedback on cGMP synthesis (Eq. 3). Due to variability in the literature concerning the values of  $B_{ca}$  and  $r_{ca}$ , we determined their values by fitting the dark–light power spectrum computed from the voltage-clamp patch recordings in darkness and in bright light shown in Fig. 3A. We obtained  $B_{ca} = 80$  and  $r_{ca} = 0.066$  (see *SI Appendix* for details), where the latter value is in agreement with experimental recordings (33, 34). We quantified the agreement between the recordings and the simulations in Fig. 3B by comparing the probability distributions (Fig. 3C) and the dark–light spectrum (Fig. 3D). Although we find very good agreement for the power spectra (Fig. 3D), the SD of the simulated current amplitude ( $\Sigma_{sim} = 2.3\%$ ) is about 15% smaller than the value for the recorded current in darkness ( $\Sigma_{dark} = 2.7\%$ ). This difference may result from instrumental noise that increases the recorded noise in darkness, which is not accounted for in the simulation. This effect is accordingly much

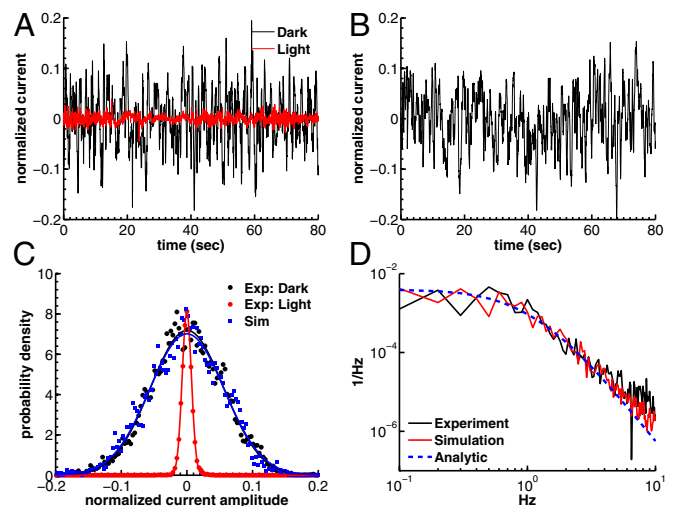


**Fig. 2.** Dark noise recordings and simulations for a GCAPs<sup>-/-</sup> mouse rod. (A) Joined currents from patch-clamp recordings from 15 rods in darkness (black) and bright light (red), filtered at 20 Hz and normalized before joining (average dark current was 16.3 pA). (B) Simulation of the normalized dark current. (C) Probability distribution of the current amplitudes from A and B together with Gaussian fits (the distribution in bright light is scaled by a factor of 7). The SDs are  $\Sigma_{dark} = 5.6\%$ ,  $\Sigma_{light} = 0.8\%$ , and  $\Sigma_{sim} = 5.6\%$ . The analytic value from Eq. 6 is 5.5%. (D) Comparison of the dark–light power spectrum from A with the power spectra from B and analytic result from Eq. 5.

larger for WT than for GCAPs<sup>-/-</sup> rods because WT rods have less intrinsic dark noise.

**Single-Photon Response for Wild-Type Mouse Rod.** We combined all of the previous results into an integrated model to simulate single-photon responses with intrinsic noise. In Fig. 4A we present 20 single-photon responses obtained from suction-electrode recordings in a WT mouse rod, which we used to validate the model. We used suction-electrode recording because cells could be held for longer times with this method, making it possible for us to obtain sufficient data from single cells over a period of several minutes (*Materials and Methods*). The data in Fig. 4A are representative of recordings from eight rods, which all gave similar results. To generate the calculated single-photon response curves shown in Fig. 4B, we used simulations of light-activated PDE from Fig. 4C. Under the conditions of our recordings, the mean time constant of decay of light-activated PDE is about 200 ms (23, 24), and the mean lifetime of excited rhodopsin is of the order of 40 ms (22, 23). Furthermore, to reconcile the experimental and simulated response amplitudes, we increased transducin activation rates by a factor of 1.75 compared with the toad simulations, which could be a result of the higher body temperature (35). This increased the average number of light-activated PDEs from a value around 6 to around 8.2 (Fig. 4C). The simulated responses in Fig. 4B show good agreement with the experimental recordings in Fig. 4A; however, the simulated dark noise ( $\Sigma_{sim} = 2.3\%$ ) is somewhat higher compared with the recorded dark noise ( $\Sigma_{dark} = 1.6\%$ ). A stronger calcium feedback with no buffering ( $B_{ca} = 1$ ) and no saturation in cGMP synthesis at high calcium concentrations ( $r_a = 0$ ) reduces both the noise level and the peak amplitude by around 50% (Fig. 4D).

### Discussion

By simulating stochastic activations of spontaneous and light-activated PDE in outer segment compartments, we generated single-photon responses together with intrinsic noise. We found that the cGMP hydrolysis rates are very different between spontaneous and light-activated PDE (see below). By analyzing

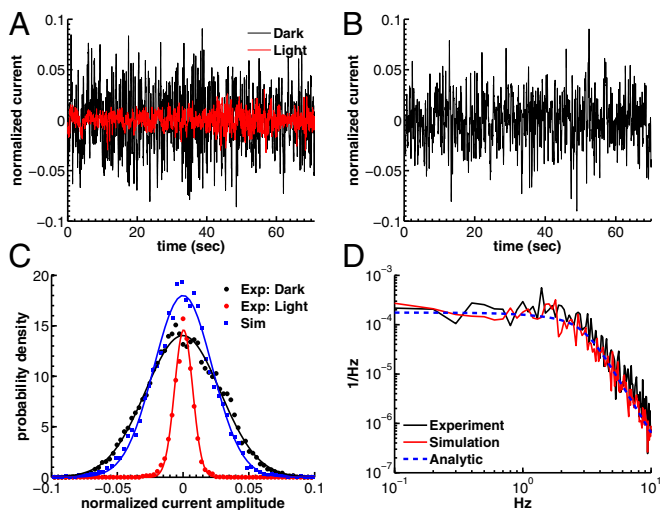


**Fig. 3.** Dark noise recordings and simulations for WT mouse rods. (A) Joined currents from patch-clamp recordings from 11 rods in darkness (black) and bright light (red), filtered at 20 Hz and normalized before joining (average dark current was 17.9 pA). (B) Simulation of normalized dark current. (C) Probability distribution of the current amplitudes from A and B together with Gaussian fits (the distribution in bright light is scaled by a factor of 4). The SDs are  $\Sigma_{dark} = 2.7\%$ ,  $\Sigma_{light} = 0.8\%$ , and  $\Sigma_{sim} = 2.3\%$ . (D) Comparison of the dark-light power spectrum obtained from A with the power spectra from B and analytic result from *SI Appendix*, Eq. 42.

electrophysiological recordings from wild-type and GCAPs<sup>-/-</sup> knockout mice, we estimated the parameters for spontaneous PDE activation and calcium feedback in a mouse rod. Our results show that a smaller outer segment enables greater temporal resolution, but a reduction in size has to be accompanied by biochemical adaptations to preserve the ability to detect single photons above background noise. We now discuss these conclusions in more detail.

**Number of Spontaneously Activated PDEs in a Compartment.** From a power spectrum analysis, we estimated that in mouse the spontaneous PDE deactivation rate is  $\mu_{sp} \approx 12.4 \text{ s}^{-1}$ , around sevenfold larger compared with its toad counterpart. Furthermore, we found a value of  $\bar{P}_{sp,comp}^* \sim 0.9$  in a mouse rod, which is similar to the value in toad. If we assume that the PDE density and the ratio  $\nu_{sp}/\mu_{sp}$  are similar in mouse and toad, a four times smaller mouse diameter would result in  $\bar{P}_{sp,comp}^* \sim 0.08$ . However, our simulations reveal that in such a case the single-photon response in mouse would be lost in the noise (Fig. 5A). This result is consistent with Eq. 5 (and with *SI Appendix*, Eqs. 44 and 53), which shows that the dark noise level (characterized by  $\Sigma_j$ ) is inversely proportional to the mean number of spontaneously activated PDEs in a compartment. Although the PDE fluctuations increase as the mean increases, the current noise decreases because PDE hydrolyzes cGMP. More spontaneously activated PDEs reduce the dark noise level and allow for a better signal-to-noise ratio at the peak single-photon response amplitude (Fig. 5B). This finding is one of the reasons why the PDE density is higher in mammalian compared with amphibian rods, because it compensates for the reduction in the number of spontaneous activated PDEs due to the much smaller disk size in mammals. The 10-fold increase from  $\bar{P}_{sp,comp}^* \sim 0.08$  to  $\bar{P}_{sp,comp}^* \sim 0.9$  is generated by a 5-fold higher PDE density (20) and a remaining factor of 2, which might be due to a stronger increase with temperature of  $\nu_{sp}$  compared to  $\mu_{sp}$  (36).

**Number of Light-Activated PDEs and Hydrolytic Activity.** Our simulations in Fig. 1 show that in a toad rod around 150 light-activated PDEs are sufficient to reduce the photocurrent by  $\sim 5\%$ . The exact number of light-activated PDEs that is needed depends on the value of  $\beta_d$  and on the amount of calcium feedback (*SI Appendix*, Figs. S8 and S9). In contrast, for a mouse rod with an activated rhodopsin decay time  $\tau_{rh} = 40 \text{ ms}$  (22, 23), already 6–10 light-activated PDEs induce such a response. We showed that this striking difference can be reconciled by assuming that the rate of cGMP hydrolysis by light-activated PDE ( $k_{li}$ ) is diffusion limited and determined by the encounter rate, in which case rod geometry plays a fundamental role. For toad, we computed  $k_{li} \sim 2.9 \text{ s}^{-1}$ , and due to the smaller diameter we obtained  $k_{li} \sim 61 \text{ s}^{-1}$  in mouse, which is similar to the estimate of  $43 \text{ s}^{-1}$  given in ref. 27. Because the rate  $k_{li}$  is so high in mouse, only very few light-activated PDEs per photon are needed to produce a response amplitude that overcomes background noise. As a consequence, the lifetime of activated rhodopsin in a mammalian rod can be much shorter than in an amphibian rod, allowing for much faster temporal resolution in mammalian rod vision.

We found that the hydrolytic rate of a spontaneously activated PDE is not diffusion limited, and from Eq. 2 we computed  $k_{sp} = 0.8 \text{ s}^{-1}$  for toad (with  $\beta_d = 1 \text{ s}^{-1}$ ) and  $k_{sp} = 4.5 \text{ s}^{-1}$  for mouse, which in both species is smaller than  $k_{li}$ . The discrepancy between  $k_{li}$  and  $k_{sp}$  is most striking for mouse, but this difference is essential, as we now show. First, a diffusion-limited hydrolysis rate  $k_{li}$  is absolutely necessary for rapid temporal resolution with few light-activated PDEs. Second, from dark noise analysis we estimated that there is on average around one spontaneously activated PDE per compartment. Thus, if  $k_{sp}$  were similar to  $k_{li}$ , this would lead to  $\beta_d \sim 55 \text{ s}^{-1}$  in a mouse rod (Eq. 2 with  $\bar{P}_{sp,comp}^* \sim 0.9$ ). Such a high rate  $\beta_d$  would require many more light-activated PDEs to induce a single-photon response amplitude that overcomes the noise level (*SI Appendix*, Fig. S7), thus impairing temporal resolution.

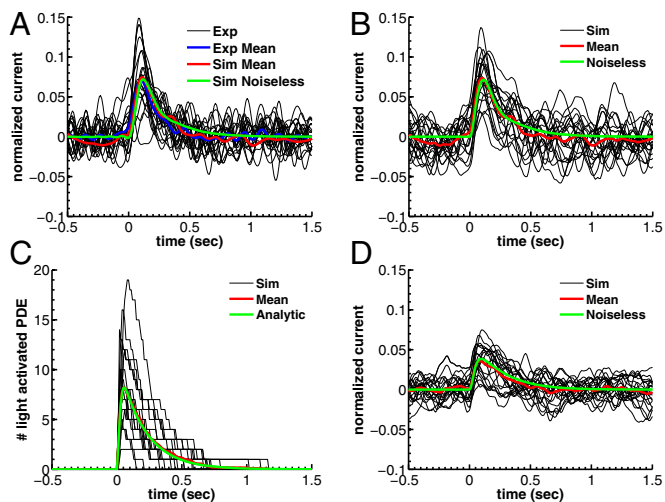


**Fig. 4.** Single-photon response for WT mouse rod. (A) Twenty suction-electrode recordings from a wild-type rod (black) with mean (blue). Currents are filtered at 20 Hz and normalized (dark current was 14.5 pA). Mean (red) and the noiseless simulation (green) from *B* are superimposed for comparison. SD of the dark current is 1.6%. Time, mean, SD, and CV of the peak current are 110 ms, 7.2%, 2.9%, and  $2.9/7.2 \approx 0.40$ . (B) Twenty single-photon response simulations (black) with mean (red) and noiseless simulation (green). Time, mean, SD, and CV of the peak current are 110 ms, 7.2%, 3.2%, and  $3.2/7.2 \approx 0.44$ . (C) Light-activated PDE (black) from *B* with mean (red) and with the analytic curve (green). Time, mean, and CV of the peak value are 55 ms, 8.2, and 0.49 (0.51 from *SI Appendix*, Eq. 58). (D) Twenty single-photon response simulations with increased calcium feedback. Parameters are as in *A* except  $B_{ca}=1$  and  $r_{ca}=0$ . SD of the dark current is 1.3%, in agreement with *SI Appendix*, Eq. 52. Mean, SD, and CV of the peak current are 3.9%, 1.8%, and  $1.8/3.9 \approx 0.46$ .

The molecular origin of the difference between  $k_{sp}$  and  $k_{li}$  is, however, an open question, which we hope that future experiments will eventually clarify.

**Impact of Calcium Feedback, Outer Segment Radius, and PDE Density on Single-Photon Response.** The photoresponse and the dark noise depend on calcium feedback (29). Increasing this feedback reduces both the amplitude of the fluctuations and the response, but does not increase reproducibility (Fig. 4D). We show this result in more detail in Fig. 5C, where we have plotted the coefficient of variation (CV) of the peak of the response as well as response amplitude and SD as a function of  $r_{ca}$ , which controls the amount of calcium feedback on the cyclase (an increase in  $r_{ca}$  decreases the feedback, Eq. 3). As feedback decreases, the amplitude and SD of the response both increase similarly, but the CV of the peak amplitude remains nearly unchanged. We conclude that calcium feedback does not alter the fidelity of the photon response, in agreement with previous results (6, 25) but in contrast to ref. 31. Nevertheless, if both calcium feedback and the number of light-activated PDEs are increased in such a way as to maintain the single-photon response amplitude, there is a better separation between the photon signal and the dark noise, but at a cost: Increasing the number of light-activated PDEs requires a longer lifetime of activated rhodopsin, reducing temporal resolution.

A smaller outer segment geometry requires fewer activated PDE molecules to produce a single-photon response. Consequently, the lifetime of an activated rhodopsin molecule in a rod with a small outer segment diameter (as in mammals) can be much shorter than in a rod with large outer segment diameter (as in amphibians), enabling a faster response and a shorter integration time. In Fig. 5D we show what happens when the radius of a toad rod photoreceptor is reduced to the size of a mouse rod, but none of the other phototransduction parameters are

changed. In this case, an abundant number of light-activated PDEs are generated that lead to response saturation around the compartment where the photon is absorbed. This leads to a much prolonged response compared with the toad or mouse single-photon response. To decrease the amount of light-activated PDE, the lifetime of activated rhodopsin has to be reduced, enabling a faster response.

However, reducing the size of the outer segment and the lifetimes of activated rhodopsin and light-activated PDE is still not sufficient to transform an amphibian into a mammalian rod. Additional adaptations in the biochemistry are needed that affect the value of  $\beta_d$  and the dark noise level. We show this result in Fig. 5E and F. Here we have reduced the outer segment PDE density of a mouse rod as in Fig. 5A and B, but we have decreased  $\beta_d$  in proportion to the decrease in PDE density. The reduction in PDE density increases both the response amplitude and the SD of the response, but it has little effect on the CV of the peak of the response (Fig. 5E). As a consequence of the reduced  $\beta_d$  value, responses become larger and decay more slowly (Fig. 5F).

To reproduce the mouse single-photon response, it is necessary to increase  $\beta_d$  to increase cGMP turnover and the temporal resolution of the response; but it is also necessary to increase the rate of spontaneous PDE activations per compartment to

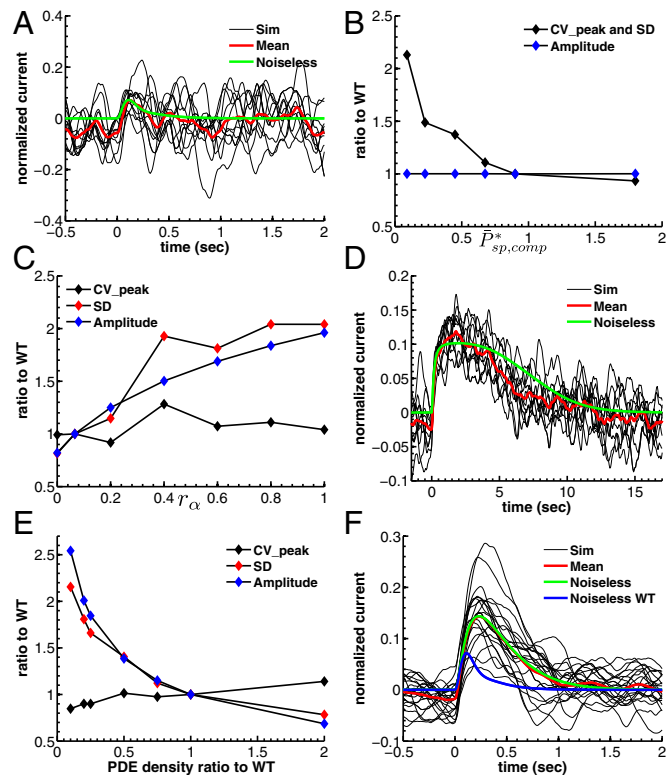


**Fig. 5.** Dependence of single-photon response on spontaneous PDE activation, cyclase feedback, PDE density, and outer segment radius. (A) Ten single-photon response simulations for a mouse rod with  $\beta_d=4.1 \text{ s}^{-1}$  and  $\bar{P}_{sp,comp}^*=0.08$ . (B) Mean, SD, and CV of the mouse peak response amplitude with respect to the WT situation depicted in Fig. 4B as a function of  $\bar{P}_{sp,comp}^*$  with constant  $\beta_d=4.1 \text{ s}^{-1}$  achieved by adapting  $k_{sp}$  (Eq. 2). Values are computed from 100 simulations. (C) Mean, SD, and CV as a function of calcium feedback on guanylyl cyclase. (D) Ten single-photon response simulations for a toad rod with a fourfold reduced OS radius and  $\beta_d=1 \text{ s}^{-1}$ .  $\bar{P}_{sp,comp}^*$  is reduced by a factor of 16, but  $k_{li}$  and  $k_{sp}$  are increased 16-fold due to the higher encounter rate. (E) Mean, SD, and CV as a function of the PDE density.  $\bar{P}_{sp,comp}^*$  and  $\beta_d$  both change ( $k_{sp}$  is unchanged). (F) Twenty single-photon response simulations for a mouse rod with fivefold reduced PDE density such that  $\beta_d=0.82 \text{ s}^{-1}$  and  $\bar{P}_{sp,comp}^*=0.18$ .

compensate for the reduction in the mean number of spontaneously activated PDEs due to the smaller radius. Both effects are achieved by increasing the PDE density. We conclude that the increase in PDE density is a key feature of adaptation in the evolution of mammalian rod photoreceptors that allows for a faster response while preserving response fidelity. However, even with all of these additional adaptations, a mouse rod has a short rhodopsin lifetime with only a few light-activated PDEs, leading to a higher variability. This might explain in part why mammals have developed additional mechanisms compared with amphibians to deal with this increased response variability, such as nonlinear thresholding at the rod-to-bipolar synapse (30, 37).

1. Yau KW, Hardie RC (2009) Phototransduction motifs and variations. *Cell* 139(2):246–264.
2. Song Z, et al. (2012) Stochastic, adaptive sampling of information by microvilli in fly photoreceptors. *Curr Biol* 22(15):1371–1380.
3. Fain G (2003) *Sensory Transduction* (Sinauer, Sunderland, MA).
4. Arshavsky VY, Burns ME (2012) Photoreceptor signaling: Supporting vision across a wide range of light intensities. *J Biol Chem* 287(3):1620–1626.
5. Baylor DA, Lamb TD, Yau KW (1979) Responses of retinal rods to single photons. *J Physiol* 288:613–634.
6. Field GD, Rieke F (2002) Mechanisms regulating variability of the single photon responses of mammalian rod photoreceptors. *Neuron* 35(4):733–747.
7. Rieke F, Baylor DA (1996) Molecular origin of continuous dark noise in rod photoreceptors. *Biophys J* 71(5):2553–2572.
8. Nikonov S, Lamb TD, Pugh EN, Jr. (2000) The role of steady phosphodiesterase activity in the kinetics and sensitivity of the light-adapted salamander rod photoresponse. *J Gen Physiol* 116(6):795–824.
9. Baylor DA, Matthews G, Yau KW (1980) Two components of electrical dark noise in toad retinal rod outer segments. *J Physiol* 309:591–621.
10. Rieke F, Baylor D (1998) Single-photon detection by rod cells of the retina. *Rev Mod Phys* 70:1027–1036.
11. Whitlock GG, Lamb TD (1999) Variability in the time course of single photon responses from toad rods: Termination of rhodopsin's activity. *Neuron* 23(2):337–351.
12. Holcman D, Korenbrot JI (2005) The limit of photoreceptor sensitivity: Molecular mechanisms of dark noise in retinal cones. *J Gen Physiol* 125(6):641–660.
13. Doan T, Mendez A, Detwiler PB, Chen J, Rieke F (2006) Multiple phosphorylation sites confer reproducibility of the rod's single-photon responses. *Science* 313(5786):530–533.
14. Hamer RD, Nicholas SC, Tranchina D, Lamb TD, Jarvinen JL (2005) Toward a unified model of vertebrate rod phototransduction. *Vis Neurosci* 22(4):417–436.
15. Hamer RD, Nicholas SC, Tranchina D, Liebman PA, Lamb TD (2003) Multiple steps of phosphorylation of activated rhodopsin can account for the reproducibility of vertebrate rod single-photon responses. *J Gen Physiol* 122(4):419–444.
16. Andreucci D, Bisegna P, Caruso G, Hamm HE, DiBenedetto E (2003) Mathematical model of the spatio-temporal dynamics of second messengers in visual transduction. *Biophys J* 85(3):1358–1376.
17. Holcman D, Korenbrot JI (2004) Longitudinal diffusion in retinal rod and cone outer segment cytoplasm: The consequence of cell structure. *Biophys J* 86(4):2566–2582.
18. Caruso G, et al. (2006) Modeling the role of incisures in vertebrate phototransduction. *Biophys J* 91(4):1192–1212.
19. Reingruber J, Holcman D (2008) Estimating the rate of cGMP hydrolysis by phosphodiesterase in photoreceptors. *J Chem Phys* 129:145102.
20. Pugh E, Jr., Lamb T (2000) Phototransduction in vertebrate rods and cones: Molecular mechanism of amplification, recovery and light adaptation. *Handbook of Biological Physics*, eds Stavenga DG, de Grip WJ, Pugh EN (Elsevier, Amsterdam), Vol 3, pp 183–255.
21. Reingruber J, Holcman D (2008) The dynamics of phosphodiesterase activation in rods and cones. *Biophys J* 94(6):1954–1970.
22. Burns ME, Pugh EN, Jr. (2009) RGS9 concentration matters in rod phototransduction. *Biophys J* 97(6):1538–1547.
23. Chen CK, Woodruff ML, Chen FS, Chen D, Fain GL (2010) Background light produces a recoverin-dependent modulation of activated-rhodopsin lifetime in mouse rods. *J Neurosci* 30(4):1213–1220.
24. Woodruff ML, et al. (2008) Modulation of phosphodiesterase6 turnover during background illumination in mouse rod photoreceptors. *J Neurosci* 28(9):2064–2074.
25. Rieke F, Baylor DA (1998) Origin of reproducibility in the responses of retinal rods to single photons. *Biophys J* 75(4):1836–1857.
26. Leskov IB, et al. (2000) The gain of rod phototransduction: Reconciliation of biochemical and electrophysiological measurements. *Neuron* 27(3):525–537.
27. Gross OP, Pugh EN, Jr., Burns ME (2012) Spatiotemporal cGMP dynamics in living mouse rods. *Biophys J* 102(8):1775–1784.
28. Reingruber J, Holcman D (2009) Diffusion in narrow domains and application to phototransduction. *Phys Rev E Stat Nonlin Soft Matter Phys* 79(3 Pt 1):030904.
29. Burns ME, Mendez A, Chen J, Baylor DA (2002) Dynamics of cyclic GMP synthesis in retinal rods. *Neuron* 36(1):81–91.
30. Okawa H, et al. (2010) Optimal processing of photoreceptor signals is required to maximize behavioural sensitivity. *J Physiol* 588(Pt 1):1947–1960.
31. Gross OP, Pugh EN, Jr., Burns ME (2012) Calcium feedback to cGMP synthesis strongly attenuates single-photon responses driven by long rhodopsin lifetimes. *Neuron* 76(2):370–382.
32. Mendez A, et al. (2001) Role of guanylate cyclase-activating proteins (GCAPs) in setting the flash sensitivity of rod photoreceptors. *Proc Natl Acad Sci USA* 98(17):9948–9953.
33. Dizhoor AM, Olshevskaya EV, Peshenko IV (2010) Mg<sup>2+</sup>/Ca<sup>2+</sup> cation binding cycle of guanylyl cyclase activating proteins (GCAPs): Role in regulation of photoreceptor guanylyl cyclase. *Mol Cell Biochem* 334(1–2):117–124.
34. Peshenko IV, Dizhoor AM (2006) Ca<sup>2+</sup> and Mg<sup>2+</sup> binding properties of GCAP-1. Evidence that Mg<sup>2+</sup>-bound form is the physiological activator of photoreceptor guanylyl cyclase. *J Biol Chem* 281(33):23830–23841.
35. Heck M, Hofmann KP (2001) Maximal rate and nucleotide dependence of rhodopsin-catalyzed transducin activation: Initial rate analysis based on a double displacement mechanism. *J Biol Chem* 276(13):10000–10009.
36. Nymark S, Heikkinen H, Haldin C, Donner K, Koskelainen A (2005) Light responses and light adaptation in rat retinal rods at different temperatures. *J Physiol* 567(Pt 3):923–938.
37. Field GD, Rieke F (2002) Nonlinear signal transfer from mouse rods to bipolar cells and implications for visual sensitivity. *Neuron* 34(5):773–785.

## Materials and Methods

The dark-noise measurements shown in Figs. 2 and 3 were obtained with patch-clamp recordings, and the single-photon responses shown in Fig. 4 with suction-electrode recordings. Simulations were run with Matlab. A detailed description of the experimental procedures and the simulation protocol is provided in [SI Materials and Methods](#) and [SI Appendix](#).

**ACKNOWLEDGMENTS.** We thank Jeannie Chen (University of Southern California) for providing the GCAPs<sup>-/-</sup> mice. This work was supported by a European Research Council Starting grant (to D.H.), National Institutes of Health (NIH) Grant EY01844 (to G.L.F.), NIH Grant EY17606 (to A.P.S.), and the McKnight Endowment Fund for Neuroscience (A.P.S.).